Reducing deformation anisotropy to achieve ultrahigh strength and ductility in Mg at the nanoscale

Qian Yu[a,b], Liang Qi[c], Raja K. Mishra[d], Ju Li[c,e], and Andrew M. Minor[a,b,1]

[a]Department of Materials Science and Engineering, University of California, Berkeley, CA 94720; [b]National Center for Electron Microscopy, Lawrence Berkeley National Laboratory, Berkeley, CA 94720; Departments of [c]Nuclear Science and Engineering and [e]Material Science and Engineering, Massachusetts Institute of Technology, Cambridge, MA 02139; and [d]General Motors Research and Development Center, Warren, MI 48090

Edited* by William D. Nix, Stanford University, Stanford, CA, and approved July 8, 2013 (received for review April 5, 2013)

In mechanical deformation of crystalline materials, the critical resolved shear stress (CRSS; τ_{CRSS}) is the stress required to initiate movement of dislocations on a specific plane. In plastically anisotropic materials, such as Mg, τ_{CRSS} for different slip systems differs greatly, leading to relatively poor ductility and formability. However, τ_{CRSS} for all slip systems increases as the physical dimension of the sample decreases to approach eventually the ideal shear stresses of a material, which are much less anisotropic. Therefore, as the size of a sample gets smaller, the yield stress increases and τ_{CRSS} anisotropy decreases. Here, we use in situ transmission electron microscopy mechanical testing and atomistic simulations to demonstrate that τ_{CRSS} anisotropy can be significantly reduced in nanoscale Mg single crystals, where extremely high stresses (~2 GPa) activate multiple deformation modes, resulting in a change from basal slip-dominated plasticity to a more homogeneous plasticity. Consequently, an abrupt and dramatic size-induced "brittle-to-ductile" transition occurs around 100 nm. This nanoscale change in the CRSS anisotropy demonstrates the powerful effect of size-related deformation mechanisms and should be a general feature in plastically anisotropic materials.

lightweight alloys | metallurgy | mechanical properties | in situ TEM | nanoparticle

Strength and ductility are critical performance indicators of materials; in metals, both are associated with the activities of line defects in the crystalline lattice, called dislocation plasticity. Ductility is accomplished by the distributed and uniform multiplication and propagation of dislocations, whereas strengthening is often achieved by hindering their motion. Strength and ductility are fundamentally linked in materials, and a mechanism to improve one almost always leads to a decrease in the other (1, 2). How to achieve both high strength and high ductility is still a challenge of great importance in structural materials. Recent work has demonstrated that it is possible to improve both strength and ductility simultaneously, but this has mostly been limited to systems with ultrafine microstructures, such as nanotwinned Cu or twinning-induced plasticity steels (3, 4).

As the lightest structural metal, Mg suffers from limited room temperature ductility and formability due to the highly anisotropic critical resolved shear stress (CRSS; τ_{CRSS}) of the different slip systems (5). In Mg, which has a hexagonal close-packed structure, the τ_{CRSS} for nonbasal (prismatic and/or pyramidal) slip is $\sim 10^2$ τ_{CRSS} for basal slip (6, 7). Such an extreme plastic anisotropy of $A \equiv \tau_{CRSS}^{nonbasal}/\tau_{CRSS}^{basal} \sim 10^2$ makes nonbasal slip very difficult to trigger. Without nonbasal slip or twinning (8), basal slip alone cannot accommodate arbitrary shape changes, and excessive basal slip in combination with unrelaxed tensile stresses in the plane-normal direction leads to spatially localized damage and rapid failure. Thus, a materials design strategy could be to enhance $\tau_{CRSS}^{basal}(D)$ greatly, where D is some tunable chemical or structural parameter, without increasing $\tau_{CRSS}^{nonbasal}(D)$ by the same proportion, which will lead to a reduced $A(D) \equiv A(D) \equiv \tau_{CRSS}^{nonbasal}/\tau_{CRSS}^{basal}$ that should give rise to latent hardening and more homogeneous plastic flow. In this regard, we are encouraged by the theoretical prediction that ideal shear strengths [theoretical upper bound to CRSS (9)] of Mg are far less anisotropic, with an anisotropy ratio of ~2 as determined from our first-principles calculations (detailed in *SI Text*). Broadly speaking, the tradeoffs between strength and ductility are well recognized in the materials science community (10, 11), so enhancing ductility by increasing both $\tau_{CRSS}^{basal}(D)$ and $\tau_{CRSS}^{nonbasal}(D)$ may sound counterintuitive. Here, we show that this strategy can indeed work and that the plastic anisotropy ratio, $A(D)$, is an essential quantity that can be engineered by nanostructuring.

The parameter D we choose to investigate experimentally is the size of a single crystal domain. As illustrated in Fig. 1*A*, according to the well established "smaller is stronger" trend (12–14), $\tau_{CRSS}^{basal}(D)$ and $\tau_{CRSS}^{nonbasal}(D)$ should both increase with decreasing D. However, because $\tau_{CRSS}^{basal}(D)$ and $\tau_{CRSS}^{nonbasal}(D)$ have upper bounds at their respective ideal shear strengths (9) at small D, an anisotropy ratio of ~100 is simply unsustainable. As such, $A(D)$ is predicted to decrease gradually from ~100 to ~2, which should facilitate more stable and homogeneous plastic flow due to interactions between more dislocation slip systems in three dimensions (i.e., latent hardening). Generally, $\tau_{CRSS} \sim \beta Gb/L + \tau_0$, where L is the dislocation free-arm length, β is dimensionless quantity ~1, G is the shear modulus, b is the Burgers vector, and τ_0 is the lattice friction (15, 16). Considering the dislocation free-arm length in coarse-grained materials is usually on the order of 10^{-6} m, the value of $\beta Gb/L$ is roughly several megapascals; thus, the huge difference between the τ_{CRSS} for basal and nonbasal slip is mainly determined by the anisotropic lattice friction stress τ_0. This has been evidenced by previous experiments and simulations, which showed $\tau_{0\text{-basal}} \approx 10^{-2}$ $\tau_{0\text{-nonbasal}}$ (17–19). Interestingly, as the grain size/sample size decreases to the same order as the dislocation free-arm length, L will become directly regulated by D so that $L \propto D^{\alpha}$, where α is a positive exponent. As grain/sample size becomes nanoscale, the value of $\beta Gb/L$ will be 10^2–10^3 times larger, and then τ_{CRSS} will no longer be determined by τ_0 but by the sample dimension (20). It is also of note that the Hall–Petch scaling $\tau_{CRSS} \sim kDa^{-\alpha} + \tau_0$ cannot stay true for very small values of D because τ_{CRSS} is limited by the ideal shear strength, when homogeneous dislocation nucleation can occur even at a temperature of 0 K (21, 22). With this physical context and the related boundary conditions for the $A(D)$ function, we expect a more isotropic and homogeneous plastic flow with dimensional refinement and strength elevation.

Author contributions: Q.Y., L.Q., R.K.M., J.L., and A.M.M. designed research; Q.Y. and L.Q. performed research; Q.Y., L.Q., R.K.M., J.L., and A.M.M. analyzed data; and Q.Y., L.Q., R.K.M., J.L., and A.M.M. wrote the paper.

The authors declare no conflict of interest.

*This Direct Submission article had a prearranged editor.

[1]To whom correspondence should be addressed. E-mail: aminor@berkeley.edu.

This article contains supporting information online at www.pnas.org/lookup/suppl/doi:10.1073/pnas.1306371110/-/DCSupplemental.

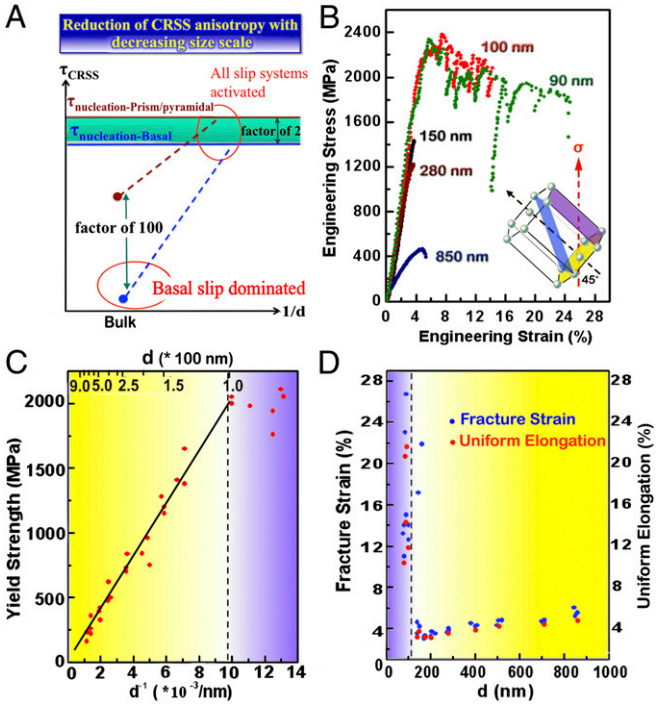

Fig. 1. (*A*) Schematic representation of the concept of reducing the CRSS anisotropy by decreasing the size scale. (*B*) Typical stress–strain curves of samples with different sizes. In addition to the "smaller is stronger" trend, the samples with extremely small size show a dramatically longer plastic stage. (*Inset*) Crystallography and loading condition are shown. (*C*) Plot of yield strength vs. the inverse of the sample gauge size d^{-1}, the power law regime, and the stress saturation regime, respectively, can be seen. (*D*) Plot of fracture strain and uniform elongation before necking vs. sample gauge size d showing a significant transition in plasticity when the sample size approaches ~100 nm.

Results

Here, we use quantitative in situ transmission EM (TEM) tensile tests on single crystal Mg samples with different sample sizes to probe directly the nanoscale size effect on the plastic anisotropy. We investigated samples that were prepared by focused ion beam (FIB) milling, followed by low-energy Ar^+ cleaning. All the experiments presented here were performed on pure Mg single crystals loaded in tension along an axis 45° from the basal plane, which is schematically shown in Fig. 1*B* (*Inset*). This orientation was chosen specifically to favor basal slip. The sample sizes ranged from ~850 nm to 80 nm. The possible Ga^+ contamination from the FIB process was analyzed before mechanical testing by high-resolution TEM characterization. The results show that the thickness of the surface damage layer resulting from the milling is about 2 nm (details are provided in *SI Text*). The detailed experimental process is described in *SI Text* as well, including examples of the initial dislocation structure (Fig. S1), where it can be seen that the size of the sample inherently limits the length of the dislocations. This method offers several advantages: (*i*) the crystal orientation can be well defined to benefit a certain slip system, and more clear analysis and comparison can be achieved; (*ii*) the dimension is the only tunable parameter (no grain boundaries or constraint from neighboring grains) and can be well controlled to regulate the length of the dislocations; (*iii*) the in situ TEM technique can provide a direct relation between the microstructural evolution and the mechanical response of a sample; and (*iv*) because we eliminated the texture effect and grain boundary effect, the fundamental mechanism can be directly assigned to the intrinsic size effect. The same results were reproduced in nanocompression tests on Mg nanoparticles (no FIB damage) and in molecular dynamics (MD) simulations, which verified the intrinsic nature of this nanoscale size effect.

Fig. 1*B* shows a comparison between typical stress–strain curves from different sample sizes. Special attention should be paid to the samples smaller than 100 nm, where ultrahigh yield stresses and significantly larger values of failure strain are observed. In addition, when calculated as true stress (shown in *SI Text*), the extended elongation in samples smaller than 100 nm actually demonstrates work hardening (shown in Fig. S2). The relation between size and strength is plotted in Fig. 1*C* (here, we define the yield strength as the stress at which the first deviation from linearity is found in the stress–strain curve). The curve first shows a power law relation, where the exponent α is around 1, until about ~100 nm, where the yield strength saturates at around 2 GPa. For comparison, we have used ab initio calculations to find the theoretical tensile strength of Mg in the tested orientation to be ~3.6 GPa (details are provided in *SI Text*), indicating that over half of the theoretical strength was achieved experimentally. Coincident with the plateau in strength, there is a significant transition in the elongation to failure, as shown in Fig. 1*D*. The values of fracture strain suddenly jump to over ~10% when the sample size is reduced to ~100 nm and reach almost 30% in specific cases, compared with 4% in larger samples. The scatter in the data might be partly due to the difficulty in precisely controlling the aspect ratio at the nanoscale. However, it is worth noting that the uniform elongation before necking should be independent of the aspect ratio. Therefore, we calculated the true stress–strain value (details are provided in *SI Text*) and plotted the uniform elongation with size (Fig. 1*D*), where the same trend of transition was observed. The corresponding deformation mechanisms that are responsible for the size-related mechanical behavior are described below.

The largest samples demonstrate work hardening and necking behavior as shown in Fig. 1*B* and Fig. 2 *A* and *B*. The strength was higher than the bulk counterpart due to the limited sources

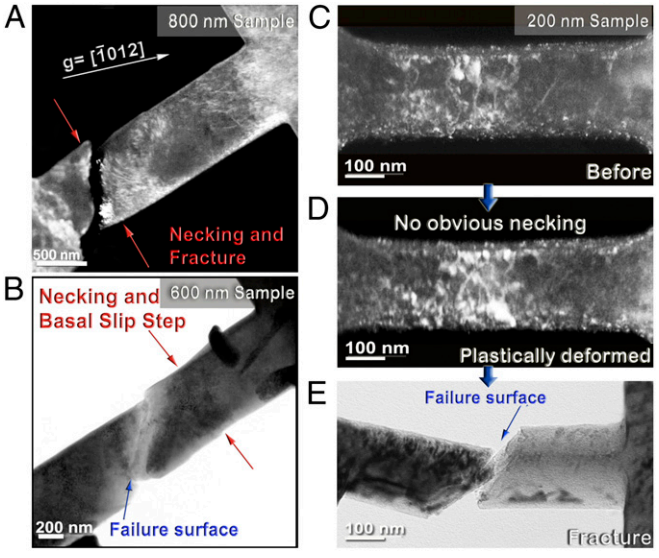

Fig. 2. (*A*) Dark field images showing the necking and failure in a sample with size ~800 nm, g = [10-12]. g, reciprocal lattice vector. (*B*) Bright field image of a deformed sample with a size of ~600 nm, where necking first happens at one place marked with red arrows and fracture occurs at another position. Dark field images (*C* and *D*) and bright field image (*E*) of a sample with a size of ~200 nm before deformation, during plastic deformation, and after fracture, respectively. Beam direction = [4-2-23].

in the confined volume. As the sample size was decreased to between ~200 and ~400 nm, the ductility became dramatically limited. Dislocation activities were much more localized (shown in Fig. 2 *C* and *D*), and failure occurred at ~3–4% engineering strain due to localized shear along the basal plane, as shown in Fig. 2*E*. So, although significant size strengthening was achieved around 200–400 nm, the plastic anisotropy, $A(D)$, remained large and the higher stresses led to rapid shear localization and poor ductility. Detailed analysis and the related movies (Movies S1–S3) are presented.

As the sample size was reduced to below ~100 nm, there was a remarkable shift in deformation behavior seen both from the stress–strain curves (Fig. 1*B*) and the in situ observations (Fig. 3). The stress vs. strain behavior shows an extremely long plastic stage with flow stresses close to ~2 GPa (and strain hardening when considering the true stress; *SI Text*). We must emphasize that the 2-GPa stress here should be compared with local stress instead of the global stress in polycrystalline materials. Comparing samples before and after the tests shows significant elongation and reduction in cross-sectional area (an example is given in Fig. 3*A* and Movie S4). Fig. 3*B* and Movie S5 show an example of the motion of a <**c** + **a**> dislocation with a Burgers vector along $[11\bar{2}3/\bar{1}2\bar{1}3]$, even though basal slip is strongly favored in this orientation (details of dislocation analysis are shown in Fig. S3). Compared with the easy glide of basal dislocations, the low mobility observed in the <**c** + **a**> dislocation during its pinning/depinning motion indicates stronger dislocation interactions and a greater likelihood of the crystal maintaining a high dislocation density during deformation. This effect would lead to a stronger dislocation interaction, creating plastic strain along both the <**a**> and <**c**> directions, and would explain the high ductility observed in this size regime. However, it is also possible to observe nonbasal slip in larger samples, as illustrated by previous studies (5, 23–25). Therefore, the critical mechanism for the improved ductility in the small size regime should be not only the activation of nonbasal slip but the relative amount of the nonbasal contribution to plastic strain. To illustrate this further, we investigated the slip steps at the surface of deformed samples in the small size regime; a typical high-resolution TEM image is shown in Fig. 3*C*. The related diffraction pattern and the crystallography viewed from this direction are shown schematically in the lower part in Fig. 3*C*, with detailed trace analysis described in *SI Text*. Importantly, it was observed that nonbasal slip steps, including both <**c**> and <**c** + **a**> slip, were found in similar amounts as basal slip. Consistent with the transition in plastic behavior in this size regime, the fracture surfaces changed to a "cup-cone" shape as shown in Fig. 3*D*, compared with the pure shear localization on the basal plane seen in the larger samples. All these observations lead one to conclude that the τ_{CRSS} anisotropy must be significantly reduced at sample sizes below 100 nm so that a full complement of slip systems, including the critically important <**c** + **a**> dislocations, is activated and significantly contributes to the plastic deformation, leading to ultrahigh strength and ductility.

To clarify further the influence of FIB damage on the results from the tensile samples, we also performed in situ TEM compression tests on FIB-free Mg nanoparticles with different sizes but of similar orientation to the tensile samples. The Mg nanoparticles were produced by a dc arc plasma method, and their

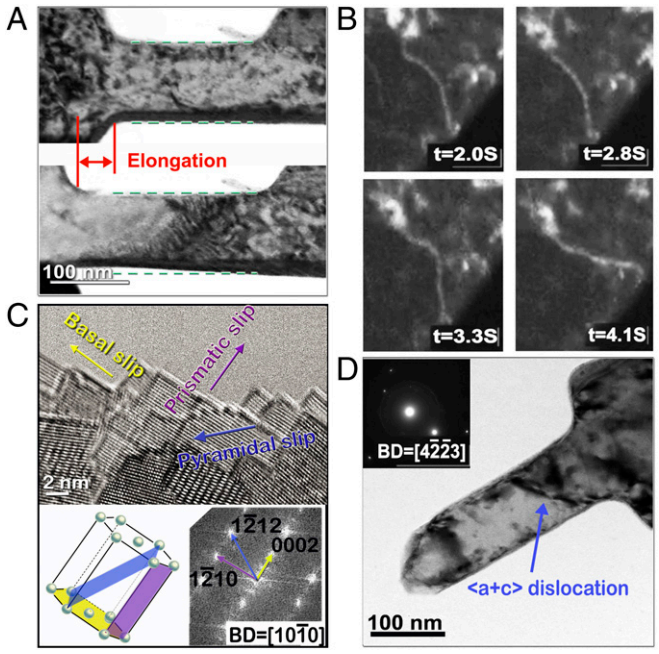

Fig. 3. (*A*) Bright field images captured from the movie of an in situ tensile test showing the large elongation and reduction in area in a sample with a size of ~100 nm. (*Upper*) Initial image of the sample is shown. (*B*) Images captured from the movie of a ~90-nm sample showing the motion of a <**c** + **a**> dislocation. (*C*) High-resolution TEM image of the slip steps at the surface of a deformed sample with a size of ~90 nm; beam direction = [10-10]. The directions for basal, prismatic (<**c**> slip), and pyramidal slips are all marked. The lower image shows the related crystallography and the related fast Fourier transform diffraction pattern for references. (*D*) Cone-shaped fracture surface in a sample with a size of ~100 nm. Beam direction = [4-2-23]. A <**c** + **a**> dislocation remained in the deformed sample.

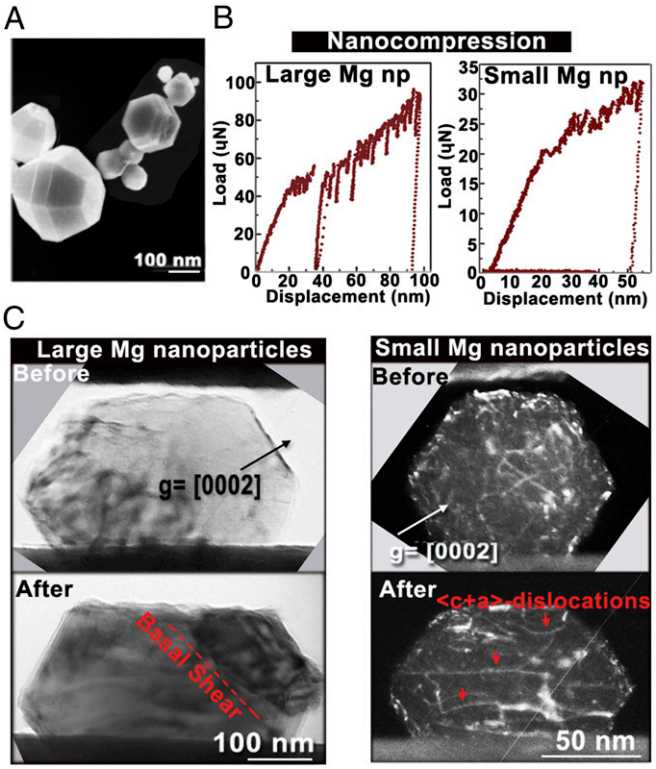

Fig. 4. (*A*) SEM image of Mg nanoparticles. (*B*) Load-displacement curves of a relatively large Mg nanoparticle (~400-nm diameter) compression (*Left*) and a small Mg nanoparticle (~100-nm diameter) compression (*Right*). (*C*) TEM images of the large particle and small particle before and after the in situ compression test. Localized shear occurred in the large particle, whereas the smaller particle deformed more homogeneously. With g = [0002], only <**c** + **a**> dislocations were visible, demonstrating the increase in <**c** + **a**> dislocation activity in the smaller particle. BD, beam direction.

sizes ranged from 700 to 50 nm (26) as shown in the SEM image in Fig. 4*A*. Details of the compression method have been described previously (27). Fig. 4*B* shows the load-displacement curves of compressing a relatively large particle and a small particle, and Fig. 4*C* displays the TEM images for a large particle and a small particle before and after compression, respectively. From the mechanical data, in situ movies (Movies S6 and S7), and diffraction analysis, it was clear that the large particles (~400 nm) mainly deformed by means of the localized shear along the basal planes, which generated significant strain bursts and a catastrophic load drop on the mechanical curve. On the other hand, the smaller particles (~100 nm) deformed through more homogeneous dislocation activity that resulted in more continuous plastic flow. The dislocation analysis in the deformed particles revealed a large number of <**c** + **a**> dislocations; no localized shear and strain bursts occurred in these particles. The strong activity of nonbasal slip in smaller particles indicated the significant reduction of CRSS anisotropy, which was consistent with the tensile results above.

Discussion

The proposed mechanism for the enhanced ductility also agrees well with our results from computational simulations. First, our generalized stacking fault (GSF) $\gamma(x)$ calculations (Fig. 5*A*) show that maximum $d\gamma/dx$ values (2.57 GPa for full basal and 1.30 GPa for partial basal and 1.99 GPa and 2.62 GPa for prismatic and pyramidal, respectively), which are good approximations of ideal shear strengths, are comparable with the ~2-GPa tensile yield stress observed in samples smaller than 100 nm, which indicates that it is energetically possible for the applied stress to overcome the dislocation nucleation barriers of all these slip systems. In addition to the energetic considerations, we investigated the dynamical behavior of dislocations by performing a series of MD simulations of tensile tests on Mg nanostructures with the same orientation as in the experiments (details are provided in *SI Text* and Figs. S4–S9). As can be seen in Fig. 5*B*, the simulation results are consistent with the experimental results, including the size-independent stress saturation and the high-level flow stresses achieved. Detailed analysis of the simulations reveals the nucleation of multiple types of dislocations even though the crystal orientation heavily favors basal slip (Fig. 5*C* and Movie S8) and also cross-slip from the basal plane to the prismatic plane. As shown in Fig. 5*D*, before eventually slipping out of the samples, different types of dislocations can interact with each other and temporarily increase the dislocation density, contributing to the plastic strain while preserving the flow stress. Another critical factor for combined ultrahigh strength and ductility is the dispersed nucleation in the smallest size regime (one example is shown in Movie S9), which facilitates more uniform deformation. From the experimental and simulation results, it can be concluded that the extremely high strength in the smallest samples can "turn on" dislocation behavior that is uncommon in bulk materials, including surface nucleation, cross-slip, and <**c** + **a**> slip, all of which strongly enhance the ductility by the reduction of plastic anisotropy. An increase in ductility at small size scales has been proposed for brittle materials, where energetic scaling laws are used to analyze fracture (28). However, in our case, the scaling of fracture does not seem to be the dominant effect, because the extensive plastic deformation we observe before planar localization would alter these energetic scaling laws so that the simple size scaling of a planar fracture criterion cannot be applied here.

Our rationale and strategy to engineer $A(D)$ should be quite general for high plastically anisotropic materials. Internal dimension refinement is one practical method for limiting the dislocation length, L, which should enhance CRSS levels and suppress $A(D)$. We believe that boundaries would also be an effective way to engineer $A(D)$ because of two special features. First, stress concentrations near boundaries result in much higher local stresses compared with the global stress, so it is possible to achieve the critical stress required to reduce deformation anisotropy; this phenomenon is more significant in nanocrystalline materials (29). Second, because of variations in atomic arrangement, grain boundaries can act as preferred sources for the nucleation and emission of dislocations (30, 31). It has been reported that Mg alloys processed by equal channel angular processing or hot rolling for grain refinement exhibit not only higher yield stresses but larger elongations at room temperature (32–34). However, conflicting results have also been reported mainly due to the texture characteristics and complication of deformation twinning (35, 36). By eliminating the complicating effects of grain boundaries and compatibility from neighboring grain orientations, our in situ TEM experiments revealed the intrinsic size dependence of plastic anisotropy and offered clear evidence that it is indeed possible to achieve both high strength and high ductility by tuning the external dimensions of the sample. The result is that the $\tau_{CRSS}(D)$ for basal and nonbasal slip can be on the same order in confined dimensions even though they are strongly anisotropic at larger sizes. Presumably, the critical dimension for this effect to manifest is material-dependent and sensitive to the chemical composition and GSF energy.

It is worth noting that the yield strength saturated when the transition occurred at 100 nm, with the stress value close to the ideal strength. The high strengths and shorter dislocation lengths can help to turn on alternative slip behavior that is not common in bulk materials (37, 38). In essence, small dimensions lead to high strengths that can activate secondary deformation mechanisms that make the deformation more uniform by promoting latent hardening and dislocation storage, leading to high ductility. More

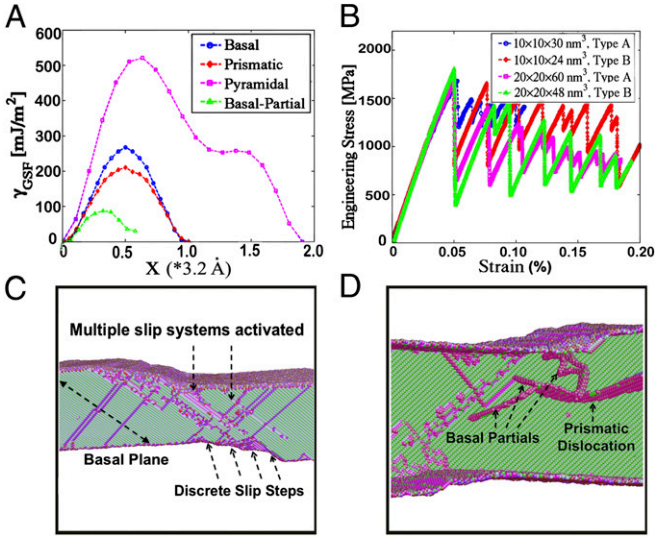

Fig. 5. (*A*) Generalized stacking fault energy curves for different slip systems. The maximum $|d\gamma/dx|$ is obtained by numerical derivations of γ(**x**). For the unsymmetrical pyramidal γ(**x**), the max $|d\gamma/dx|$ depends on slip direction, and we choose the direction with the lower $|d\gamma/dx|$. (*B*) Typical stress–strain curves from MD simulations of several samples, whose basal plane is 45° off the tensile axis (detailed sample configurations and orientations are provided in *SI Text*). All samples can reach 20% strain by dislocation plasticity, except for type A, which resulted in a twin event at 10% strain. (*C*) A 20 × 20 × 60-nm^3 sample after 20% strain, which shows slip on different types of planes and obvious necking. Here, the different colors refer to different coordination numbers, so that the tracks of dislocations on the surface can be observed clearly. (*D*) Interaction of basal and nonbasal dislocations inside the MD sample of *C*. Only atoms with coordination numbers that are not perfect are shown.

broadly, we have revealed the size dependence of plastic anisotropy and the intrinsic nanoscale size effect of the reduction in plastic anisotropy to show that high strengths can be beneficial for ductility and formability in plastically anisotropic materials.

Materials and Methods

Single crystal Mg and Mg nanoparticles are tested under tension and compression, respectively. The crystal orientations of each are chosen to favor basal slip. Detailed materials and methods are described in *SI Text*, including dislocation analysis, deformation characteristics, trace analysis of the slip steps, and details of the density functional theory and MD calculations.

ACKNOWLEDGMENTS. We thank X. Q. Zeng for providing the nanoparticles used in this study and R. O. Ritchie for valuable discussions. L.Q. and J.L. acknowledge support by National Science Foundation Grants DMR-1120901 and DMR-1008104. This research was supported by the General Motors Research and Development Center and was performed at the National Center for Electron Microscopy at Lawrence Berkeley National Laboratory, which is supported by the US Department of Energy under Contract DE-AC02-05CH11231.

1. Malygin GA (2007) Plasticity and strength of micro- and nanocrystalline materials. *Phys Solid State* 49:1013–1033.
2. Yip S (2004) Nanocrystalline metals: Mapping plasticity. *Nat Mater* 3(1):11–12.
3. Frommeyer G, Brux U, Neumann P (2003) Supra-ductile and high-strength manganese-TRIP/TWIP steels for high energy absorption purposes. *ISIJ Int* 43(3):438–446.
4. Lu K, Lu L, Suresh S (2009) Strengthening materials by engineering coherent internal boundaries at the nanoscale. *Science* 324(5925):349–352.
5. Agnew SR, Duygulu O (2005) Plastic anisotropy and the role of non-basal slip in magnesium alloy AZ31B. *Int J Plast* 21(6):1161–1193.
6. Hutchinson WB, Barnett M (2010) Effective values of critical resolved shear stress for slip in polycrystalline magnesium and other hcp metals. *Scr Mater* 63(7):737–740.
7. Koike J, et al. (2003) The activity of non-basal slip systems and dynamic recovery at room temperature in fine-grained AZ31B magnesium alloys. *Acta Mater* 51(7): 2055–2065.
8. Yu Q, et al. (2012) The nanostructured origin of deformation twinning. *Nano Lett* 12(2):887–892.
9. Zhu T, Li J (2010) Ultra-strength materials. *Prog Mater Sci* 55(7):710–757.
10. Ritchie RO (2011) The conflicts between strength and toughness. *Nat Mater* 10(11): 817–822.
11. Zhu YT, Liao XZ (2004) Nanostructured metals: Retaining ductility. *Nat Mater* 3(6): 351–352.
12. Kumar KS, Van Swygenhoven H, Suresh S (2003) Mechanical behavior of nanocrystalline metals and alloys. *Acta Mater* 51(19):5743–5774.
13. Uchic MD, Dimiduk DM, Florando JN, Nix WD (2004) Sample dimensions influence strength and crystal plasticity. *Science* 305(5686):986–989.
14. Richter G, et al. (2009) Ultrahigh strength single crystalline nanowhiskers grown by physical vapor deposition. *Nano Lett* 9(8):3048–3052.
15. Parthasarathy TA, Rao SI, Dimiduk DM, Uchic MD, Trinkle DR (2007) Contribution to size effect of yield strength from the stochastics of dislocation source lengths in finite samples. *Scr Mater* 56(4):313–316.
16. Orowan E (1948) Symposium on internal stresses. *Metals and Alloys* (Institute of Metals, London), p 451.
17. Sun DY, et al. (2006) Crystal-melt interfacial free energies in hcp metals: A molecular dynamics study of Mg. *Physical Review B* 73(2):024116–024128.
18. Reed-Hill RE, Robertson WD (1957) Deformation of magnesium single crystals by nonbasal slip. *Transactions of the American Institute of Mining and Metallurgical Engineers* 9:496–502.
19. Conrad H, Robertson WD (1957) Effect of temperature on the flow stress and strain-hardening coefficient of magnesium single crystals. *Transactions of the American Institute of Mining and Metallurgical Engineers* 209:503.
20. Huang L, et al. (2011) A new regime for mechanical annealing and strong sample-size strengthening in body centred cubic molybdenum. *Nat Commun* 2:547–552.
21. Ogata S, Li J, Yip S (2002) Ideal pure shear strength of aluminum and copper. *Science* 298(5594):807–811.
22. Weinberger CR, Cai W (2012) Plasticity of metal nanowires. *J Mater Chem* 22: 3277–3292.
23. Obara T, Yoshinga H, Moroaumi S (1973) {11-22} [-1-123] Slip system in magnesium. Acta Metallurgica 21:845–853.
24. Meyers MA, Mishra A, Benson DJ (2006) Mechanical properties of nanocrystalline materials. *Prog Mater Sci* 51:427–556.
25. Lilleodden E (2010) Microcompression study of Mg (0001) single crystal. *Scr Mater* 62(8):532–535.
26. Stéphane P, Zou JX, Zeng XQ, Sun HQ, Ding WJ (2012) Preparation and hydrogen storage properties of ultrafine pure Mg and Mg-Ti particles. *Transactions of Nonferrous Metals Society of China* 22:1849–1854.
27. Shan ZW, et al. (2008) Ultrahigh stress and strain in hierarchically structured hollow nanoparticles. *Nat Mater* 7(12):947–952.
28. Gao HJ, Ji BH, Jager IL, Arzt E, Fratzl P (2003) Materials become insensitive to flaws at nanoscale: Lessons from nature. *Proc Natl Acad Sci USA* 100(10):5597–5600.
29. Reimann K, Würschum R (1997) Distribution of internal strains in nanocrystalline Pd studied by x-ray diffraction. *J Appl Phys* 81:7186–7192.
30. Capolungo L, et al. (2007) Dislocation nucleation from bicrystal interfaces and grain boundary ledges: Relationship to nanocrystalline deformation. *J Mech Phys Solids* 55:2300–2327.
31. Yamakov V, Wolf D, Phillpot SR, Mukherjee AK, Gleiter H (2002) Dislocation processes in the deformation of nanocrystalline aluminium by molecular-dynamics simulation. *Nat Mater* 1(1):45–48.
32. Hanzi AC, et al. (2009) Design strategy for microalloyed ultra-ductile magnesium alloys. *Philos Mag Lett* 89(6):377–390.
33. Kim WJ, Jeong HG, Jeong HT (2009) Achieving high strength and high ductility in magnesium alloys using severe plastic deformation combined with low-temperature aging. *Scr Mater* 61(11):1040–1043.
34. Mukai T, Yamanoi M, Watanabe H, Higashi K (2001) Ductility enhancement in AZ31 magnesium alloy by controlling its grain structure. *Scr Mater* 45(1):89–94.
35. Gan WM, et al. (2009) Microstructure and tensile property of the ECAPed pure magnesium. *Journal of Alloys and Compounds* 470:256–262.
36. Kim WJ, Jeong HT (2005) Grain-size strengthening in equal-channel-angular-pressing processed AZ31 Mg alloys with a constant texture. *Mater Trans* 46:251–258.
37. Akasheh F, Zbib HM, Hirth JP, Hoagland RG, Misra A (2007) Dislocation dynamics analysis of dislocation intersections in nanoscale metallic multilayered composites. *J Appl Phys* 101(8):084314–084323.
38. Demkowicz MJ, Wang J, Hoagland RG (2008) Interfaces between dissimilar crystalline solids. *Dislocations in Solids*, ed Hirth JP (Elsevier, Amsterdam), Vol 14, pp 141–205.

Supporting Information

Yu et al. 10.1073/pnas.1306371110

SI Text

1. Experimental Methods and Dislocation Analysis in Undeformed Samples with Different Sizes

All the experiments presented here were performed on a 99.999% pure Mg single crystal loaded along a direction 45° from the basal plane. For a conventional bulk counterpart, basal slip is dominant (1).

Submicron-sized tension specimens were fabricated with an FEI Strata 235 Dual Beam focused ion beam (FIB). The tensile samples were fabricated to be 80–900 nm wide with a thickness similar to the value of the width. To mitigate any effects from FIB damage, all samples were further milled with a Fischione 1040 NanoMill with a low-energy (1–2 kV) Ar^+ source. Low-energy ion beam cleaning was used to remove the damage layer induced by FIB. Fig. S1 shows the high-resolution transmission EM (HRTEM) images of a tensile sample before the test. The surface-damaged layer observed is thinner than 2 nm. The Mg lattice is well aligned even in the region that is close to the surface, as shown in Fig. S1*A*. The in situ TEM uniaxial tensile tests were performed with a JEOL 3010 transmission electron microscope with a Hysitron Picoindenter, similar to previous studies (2). The diamond tensile tips were fabricated by FIB. All the tests were conducted under displacement control mode with strain rate of about 1×10^{-3} per second to 8×10^{-4} per second. After the in situ tensile tests, the sample was further thinned down for HRTEM imaging with a 1-kV Ar^+ ion beam. The HRTEM study was performed with a Philips CM300FEG transmission electron microscope at 300 kV and an FEI Technai F20 microscope at 200 kV. Fig. S1 *B–D* shows the original dislocation structures in samples with different sizes.

2. True Stress Example

To demonstrate that strain hardening is observed in the smallest samples, Fig. S2 shows Fig. 1*B* with the true stress values calculated periodically for the 90-nm sample. The true stress was calculated by measuring the instantaneous contact area (assuming constant thickness) from the video of each experiment, respectively. Uniform elongation corresponds to the strain up to plastic instability (necking).

3. Deformation Behavior of Larger Samples

The largest samples demonstrate "bulk-like" strain-hardening behavior in their stress–strain curve as well as in their in situ deformation behavior. Combining the mechanical data (one example is shown in the stress–strain curve of the 800-nm sample in Fig. 1*B* and Movie S1), it can be clearly seen that dislocation activities initialized after a short elastic stage and then operated in the whole-gauge section, contributing to continuous strain hardening. Plastic instability was reached at ∼500 MPa, at which point the sample necked and shortly ran to failure. The image in Fig. 2*A* shows a typical fracture event in this general size regime, where rough fracture surfaces can be seen. These phenomena indicate that 3D dislocation activities were present; dislocation multiplication and interaction still dominated the plastic deformation in this size regime, however. When the sample size was decreased to about 600 nm, the mechanical behavior was generally the same as in the larger samples, demonstrating hardening and necking. However, with presumably fewer preexisting dislocations than in the larger samples, we found that the necking may take place in more than one location (Fig. 2*B* and Movie S2), indicating the effect of the exhausting hardening. The strength of materials increased with decreasing size in this regime.

As sample sizes decrease to between ∼200 nm and ∼400 nm, the number of preexisting dislocations decreases and less plasticity can be seen. The related stress–strain curves are usually composed of a long elastic stage and a short strain-hardening stage; from the related movies (Movie S3, for one example), dislocation activities were much more localized, followed by fracture (shown in Fig. 2 *C–E*), which happened at ∼3–4% engineering strain. The fracture surfaces in this size regime become much flatter and are precisely situated at ∼45° from the tensile direction. This is believed to be mainly due to the shear localization by localized 2D dislocation activities, where a dislocation source operates on certain nearby crystal planes (basal planes in our tests), generating numbers of dislocations with the same type. These dislocations quickly slip out and produce appreciable shear along the direction of sliding, resulting in fracture along the basal planes. Due to the limited elongation, single dislocation movement is hard to capture. As the sample size further decreases, the hardening region becomes shorter or even undetectable, such as the 150-nm curve shown in Fig. 1*B*.

4. G·b Analysis on the Dislocations in a Deformed Sample with Size ∼100 nm

Beam direction (BD) values of [01-11] and [01-12] were used in this G·b analysis. The dislocation was visible under g (reciprocal lattice vector) = [−1,011], [1-101], [2-1-10], and [01-1-1], as shown in Fig. S3. Thus, the Burgers vector of the dislocation will be of **c** + **a** type with **b** either [11-2-3] or [-12-13].

5. Trace Analysis of the Slip Steps

Related to Fig. 3*C*, the plane on which we labeled "basal slip" is perpendicular to the connection between [0000] and [0002] reflection spots. The 2D projected morphology of the steps can be clearly seen, and the orientations of these slip steps were analyzed by trace analysis. Slip steps on the basal plane can be seen perpendicular to the direction of the [0002] reflection. Many other slip steps are seen at angles that would represent pyramidal and prismatic slip. Some of them are rotated nearly 90° from the basal slip and perpendicular to the line between [000] and the [1-210] reflection spot, so that they are labeled as prismatic slip. The angle between some other steps and the line between [0000] and the [1-212] reflection spot are about 79–82°, which most likely corresponds to pyramidal slip.

6. Density Functional Theory Calculation of Ideal Strength of Mg

Density functional theory (DFT) calculations were performed using the Vienna ab initio simulation package (3). All the calculations were performed in a non–spin-polarized condition, and two different types of pseudopotentials were applied: One is the projector augmented wave (PAW) method with the Perdew–Burke–Ernzerhof (PBE) exchange-correlation functional (4, 5), and the other is ultrasoft (6) pseudopotential with the generalized gradient approximation functional (GGA) (7). Monkhorst–Pack **k**-point grids for the Brillouin-zone integration were applied with a **k**-point density higher than 18 per angstrom along each periodic direction in reciprocal space. Partial occupancies of eigenstates were determined by a first-order Methfessel–Paxton smearing of $\sigma = 0.2$ eV. The cutoff energy for the plane wave basis was 400 eV. The relaxed shear stress–strain relation of Mg on the basal plane along the [11-20] direction is calculated

and plotted in Fig. S4. It shows that the ideal shear stress under such orientation is ~1.8 GPa. If we assume the Schmid factor is 0.5 in our tensile tests, the ideal tensile stress should be ~3.6 GPa.

7. DFT Calculation of Generalized Stacking Fault of Mg

We performed DFT calculations to obtain generalized stacking fault (GSF) energy surfaces of Mg. The calculation methods and parameters were the same as those in the DFT calculation of Mg ideal strength (PAW-PBE potential with cutoff energy equal to 210 eV), except that different supercell configurations were used (Fig. S5). Here, three typical slip systems were investigated: {0001}<11-20> (basal), {1-100}<11-20> (prismatic), and {11-22}<11-2-3> (pyramidal). The supercells were constructed by (1 × 1) periodicity of the slip plane with the x axis along the Burgers vector and the y axis perpendicular to it; along the z axis, there were 16 layers of slabs (20 layers for pyramidal) plus a 13-Å vacuum. Thus, there were 32 atoms for basal/prismatic supercells and 40 atoms for pyramidal supercells. For basal/prismatic supercells, 16 × 10 × 1 **k**-point grids were used, and for pyramidal supercells, 9 × 10 × 1 **k**-point grids were used. During GSF calculations, a fault vector **x** was applied by shifting the top half of supercells rigidly along the Burgers vector (x axis). In addition, GSF energies of partial basal dislocation were investigated by shifting along the <1-100> direction (y axis) for basal slip supercells. Under these fault vectors, DFT calculations were performed by relaxing all atoms only along the z axis. GSF results were obtained as follows:

$$\gamma(\mathbf{x}) = (E(\mathbf{x}) - E_0)/\mathrm{A}.$$

Here, $\gamma(\mathbf{x})$ is GSF energy for fault vector **x**; $E(\mathbf{x})$ and E_0 are the energy of a supercell with fault vector **x** and a supercell with a perfect lattice, respectively; and A is the area of the slip plane. The results are shown in Fig. 5*A*. Finally, to evaluate the ideal shear strengths for different slip systems, the maximum slope of $\gamma(x)$ ($|d\gamma/dx|$) is obtained by taking numerical derivations of polynomial fitted curves of $\gamma(x)$. For the unsymmetrical pyramidal $\gamma(x)$, the max $|d\gamma/dx|$ depends on slip direction, and we choose the direction with the lower $|d\gamma/dx|$. Fig. S6 also shows the full GSF on prismatic and pyramidal planes, which confirms that the easiest slip is along the <11-20> and <11-23> directions on the {1-100} and {11-22} planes, respectively, without partial dislocations.

8. Molecular Dynamics Simulations of Tensile Tests of Mg Nanowires

Molecular dynamics (MD) simulations were performed by large-scale atomic/molecular massively parallel simulator (LAMMPS) to investigate the deformation mechanism in tensile tests of Mg single crystals along a direction 45° to the basal plane. embedded atom method (EAM) interatomic potential for Mg was applied (8). The rectangular-shaped samples with a periodic boundary condition along the z axis were made according to two different orientations of MD samples, as shown in Fig. S7. For each orientation, two different sizes (10 × 10 nm^2 and 20 × 20 nm^2) were applied to check the size effects. All the tensile tests were performed at a temperature of 300 K, and MD relaxation of 1 ns under 300 K was performed before each tensile test. The strain rate was 2×10^7 s^{-1}, and the maximum strain was 0.2. Finally, to illustrate clearly the dislocation activities, 50 steps of conjugate gradient minimization were performed for each output atomic configuration, which would eliminate the changes of atomic coordination number due to local thermal fluctuation but would not change the structures of dislocations.

The stress–strain results are shown in Fig. S8. After yielding, each sample can reach a strain of 0.2 without failure facilitated by continuously surface-nucleated dislocations, which would quickly slip out of the samples. The only exception is the 10 × 10-nm^2 sample with type A orientation, where twin nucleation occurred when the strain reached 0.1; thus, we did not plot the stress after 0.1 strain. As can be seen in Fig. S8, the simulation results are remarkably similar to the experiment results in a number of ways:

i) Young's modulus under such orientation is 37.4 GPa, and the experiment value is ~40 GPa.

ii) The yielding corresponds to the first nucleation of dislocation from the corner of surfaces in simulations, which happens at ~1.8 GPa, followed by a load drop, compared with the experiment results, which give an average yield stress of ~2 GPa.

iii) The yield stress saturated in our experimental samples with a size ≤100 nm and in MD samples. This is consistent with previous theoretical studies that showed the weak size dependence of the stress for surface nucleation of dislocations (9, 10).

iv) The flow stress can almost stay at an ultrahigh level, close to that of yield stress.

The atomic configurations of samples after deformation are shown in Fig. S9.

Two tendencies can be generalized based on these samples. First, both basal and nonbasal slip systems can be activated in most cases, and their interactions can increase the strength and ductility of samples in real tensile tests (dislocation nucleation and interactions during the whole tensile test are clearly shown in Movie S8). As shown in Fig. S9, there are many tracks left by dislocation lines that are not on the basal planes, especially those under greater strain. Detailed analyses show that all these nonbasal dislocations in MD simulations are from prismatic slips. In experiments, we indeed observed basal, prismatic, and pyramidal slips. However, we have not observed pyramidal slip in MD simulations, possibly because of the inaccuracy of classical MD potential to describe <**c** + **a**> behaviors. Nevertheless, to show the emergence of large amounts of prismatic slips in MD simulations successfully is still a critical step to demonstrate that high stress can reduce deformation anisotropy, because prismatic slip also has critical resolved shear stress ~100-fold that of its counterpart of basal slip, such that its strong activation was not expected to occur frequently in bulk Mg under normal stress conditions. We expect that pyramidal slip can also be observed for the same reason with more accurate MD potential. Second, smaller samples have more homogeneous distributions of dislocation nucleation sites, resulting in more uniform deformation. We can see dislocations nucleate from multiple places; especially in smaller samples (Fig. S9 *A* and *B*), the distributions of dislocation nucleation locations are more homogeneous than in larger samples (Fig. S9 *C* and *D*). Especially for 10 × 10 × 30-nm^3 sample with type A orientation, there is only one partial dislocation pair on the basal plane nucleated at each nucleation site (Movie S9), and each basal dislocation nucleation corresponds to each stress drop event in the stress–strain curve; thus, it has the highest average flow stress, as shown in Fig. S8. In conclusion, interactions of multiple slip systems and a homogeneous distribution of dislocation nucleation result in uniform deformation, high flow stress, and ductile failure of very small Mg samples. We can clearly see this trend in Fig. S8, which suggests that 10 × 10-nm^2 samples have a higher average flow stress than 20 × 20-nm^2 samples.

1. Ulacia I, et al. (2010) Mechanical behavior and microstructural evolution of a Mg AZ31 sheet at dynamic strain rates. *Acta Materialia* 58(8):2988–2998.
2. Yu Q, et al. (2012) The nanostructured origin of deformation twinning. *Nano Lett* 12(2):887–892.
3. Kresse G, Furthmüller J (1996) Efficient iterative schemes for ab initio total-energy calculations using a plane-wave basis set. *Phys Rev B Condens Matter* 54(16):11169–11186.
4. Blöchl PE (1994) Projector augmented-wave method. *Phys Rev B Condens Matter* 50(24):17953–17979.
5. Perdew JP, Burke K, Ernzerhof M (1996) Generalized gradient approximation made simple. *Phys Rev Lett* 77(18):3865–3868.
6. Vanderbilt D (1990) Soft self-consistent pseudopotentials in a generalized eigenvalue formalism. *Physical Review B* 41(11):7892–7895.
7. Perdew JP, et al. (1992) Atoms, molecules, solids, and surfaces: Applications of the generalized gradient approximation for exchange and correlation. *Physical Review B* 46(11):6671–6687.
8. Liu XY, Adams JB, Ercolessi F, Moriarty JA (1996) EAM potential for magnesium from quantum mechanical forces. *Modelling and Simulation in Materials Science and Engineering* 4(3):293–303.
9. Zhu T, Li J, Samanta A, Leach A, Gall K (2008) Temperature and strain-rate dependence of surface dislocation nucleation. *Phys Rev Lett* 100(2):025502.
10. Cahn RW (1954) Twinned crystals. *Adv Phys* 3:363–445.

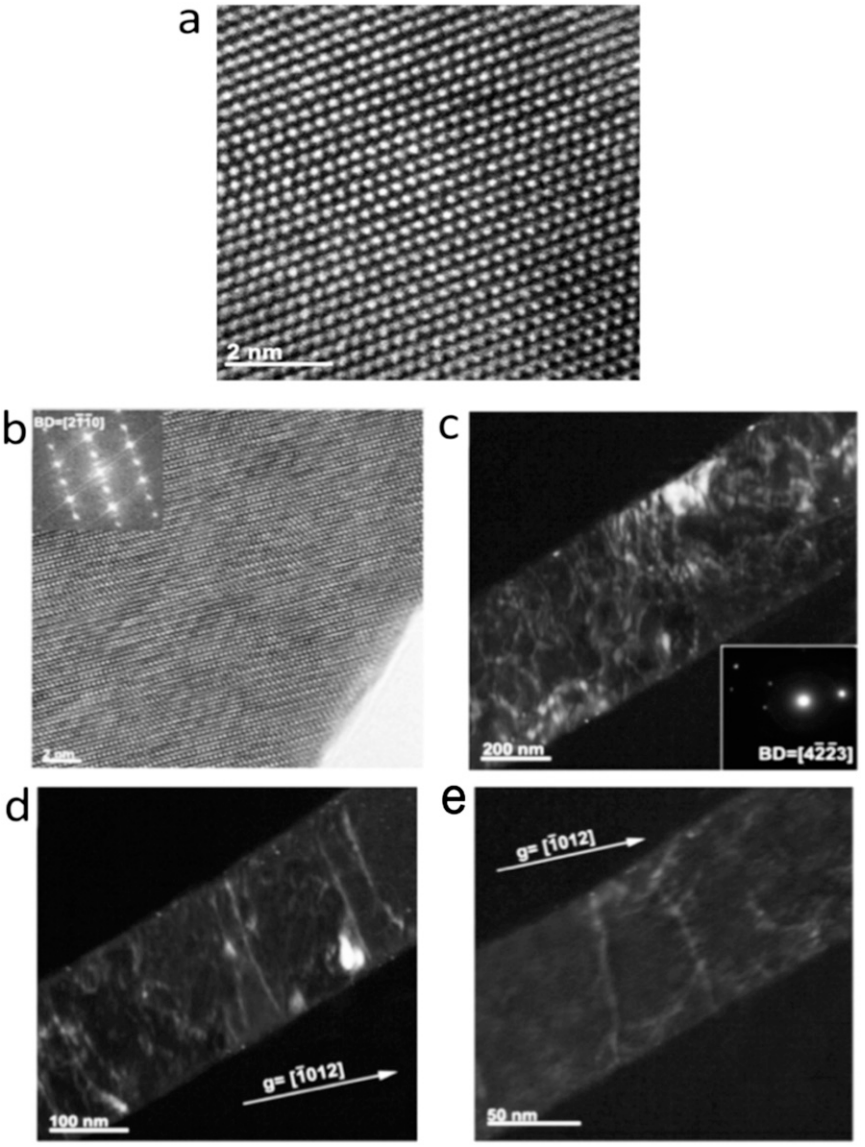

Fig. S1. (*A*) HRTEM image taken from the region that is close to the edge of a prepared 100-nm sample. (*B*) HRTEM image taken from the edge of a prepared sample. (*C–E*) Dark field images showing the dislocation structure before the tension tests in samples with a size of ~600 nm, 200 nm, and 90 nm, respectively (g = [−1,012]). *C*, *Inset* shows corresponding diffraction pattern. The smaller samples clearly show that the dislocation length is limited by the size of the sample. BD, beam direction; g, reciprocal lattice vector.

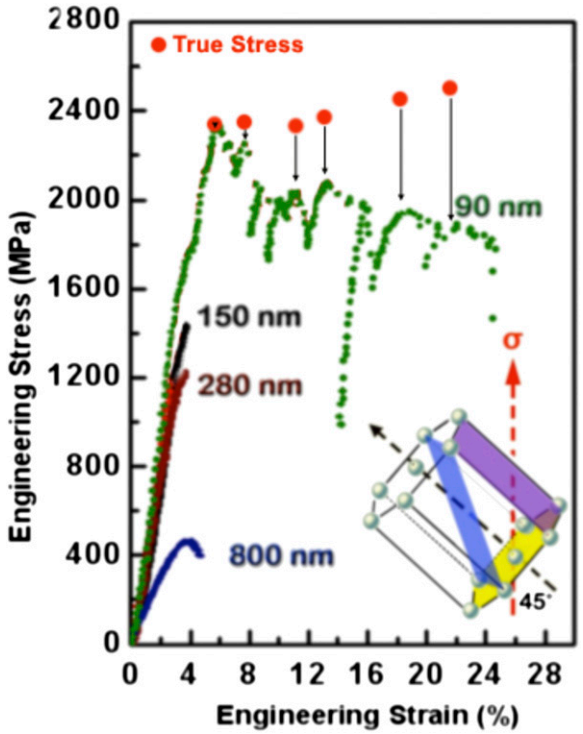

Fig. S2. The engineering strain–stress curves with the true stress for the 90-nm sample calculated, with the instantaneous contact area marked with red dots. The *Inset* is the schematic of the sample orientation and loading condition.

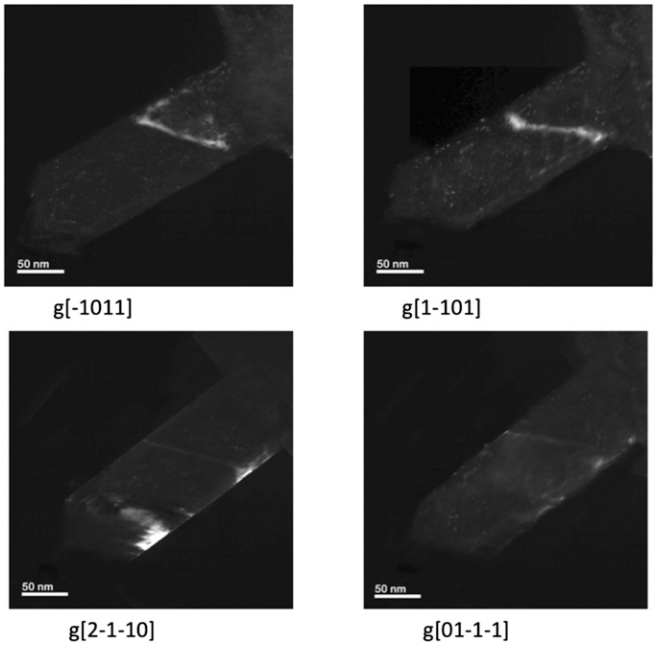

Fig. S3. Dark field TEM images of a <**c** + **a**> dislocation under different g vectors. g, reciprocal lattice vector.

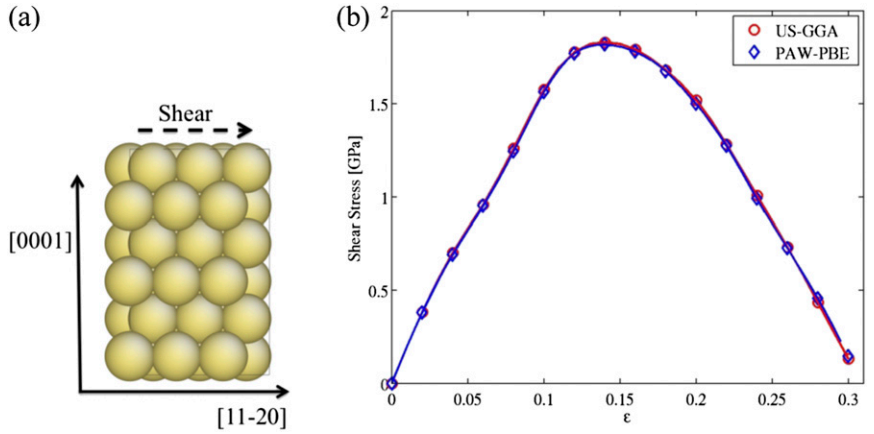

Fig. S4. (*A*) Configuration of a supercell with six (0001) layers of Mg. Shear is applied along the [11-20] direction on the (0001) plane. (*B*) Relaxed shear stress–strain relation of Mg calculated by a Vienna ab initio simulation package based on the supercell in *A* and two different pseudopotentials. US-GGA, ultrasoft generalized gradient approximation.

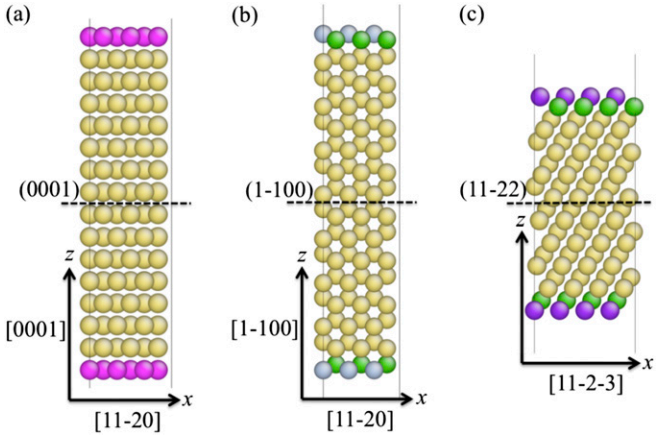

Fig. S5. Supercell configurations for Mg GSF calculations. The basal (*A*), prismatic (*B*), and pyramidal (*C*) slip systems are shown. Colors of atoms mean coordination number. Yellow means coordination number = 12 so that the atom is in the bulk; atoms with other colors are on the surfaces. All the atoms above the dashed lines (slip plane) are shifted rigidly during GSF calculations.

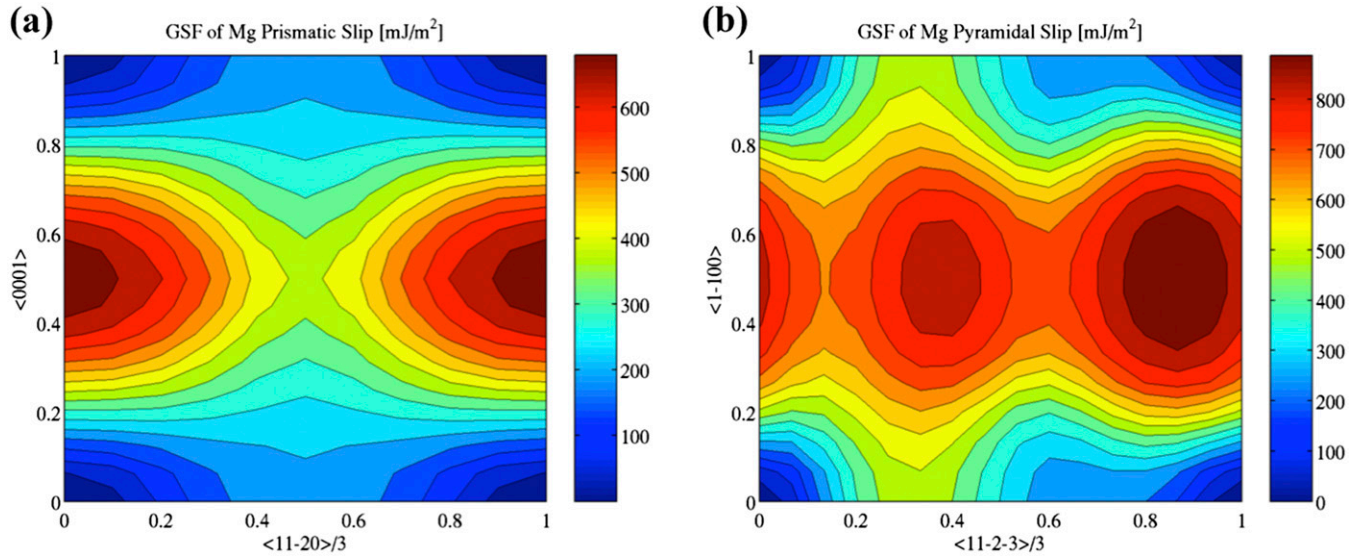

Fig. S6. GSF of Mg on prismatic (*A*) and pyramidal (*B*) planes.

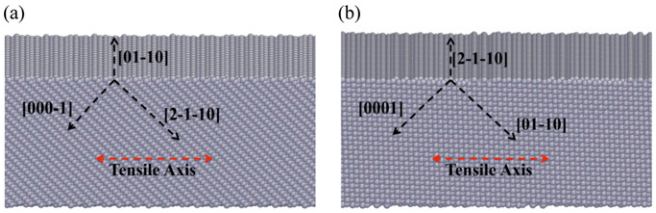

Fig. S7. MD samples with two different types of orientations. In both samples, the basal plane has an angle of 45° with the tensile axis. (*A*) In type A, one <a>-axis ([2-1-10]) has an angle of 45° with the tensile axis, so the corresponding slip system has the highest Schmid factor of 0.5. (*B*) In type B, one <a> axis ([2-1-10]) has an angle of 90° with the tensile axis, so the corresponding slip system has a Schmid factor of 0. However, the other two a axes ([-12-10] and [-1-120]) have a Schmid factor smaller than 0.5.

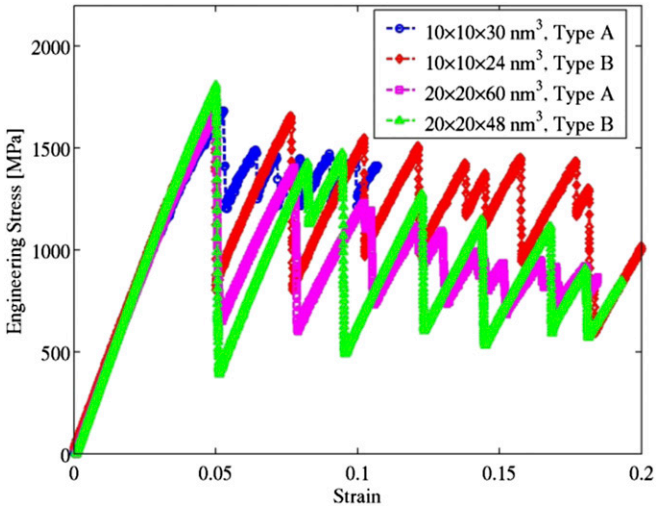

Fig. S8. Stress–strain curves from MD samples with different types of orientations (as indicated in Fig. S7) and different sizes.

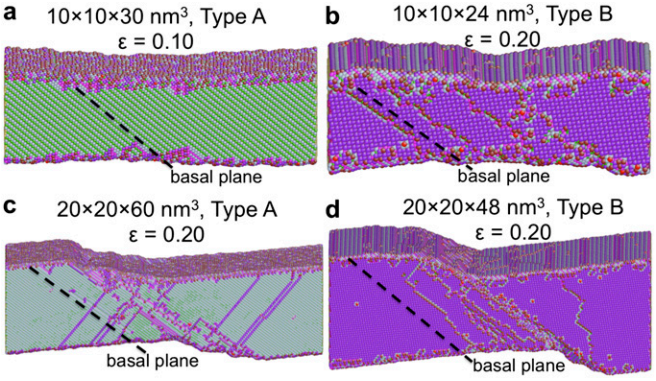

Fig. S9. (*A–D*) Atomic configurations of samples after deformation. Here, different colors mean different coordinate numbers, so the tracks of dislocation lines on the surfaces can be observed clearly. Basal slips result in tracks on the surface along basal planes, and prismatic slips produce tracks on the surface perpendicular to basal planes. (*D*) Cross-slip of <**a**> dislocations was also observed, as shown on the right side of this figure.

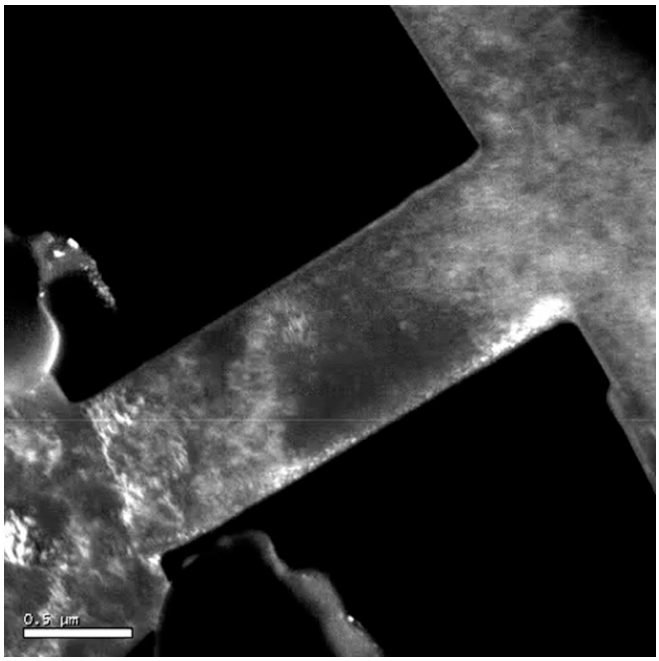

Movie S1. In situ TEM tensile test of a sample with an 800-nm gauge section.

Movie S1

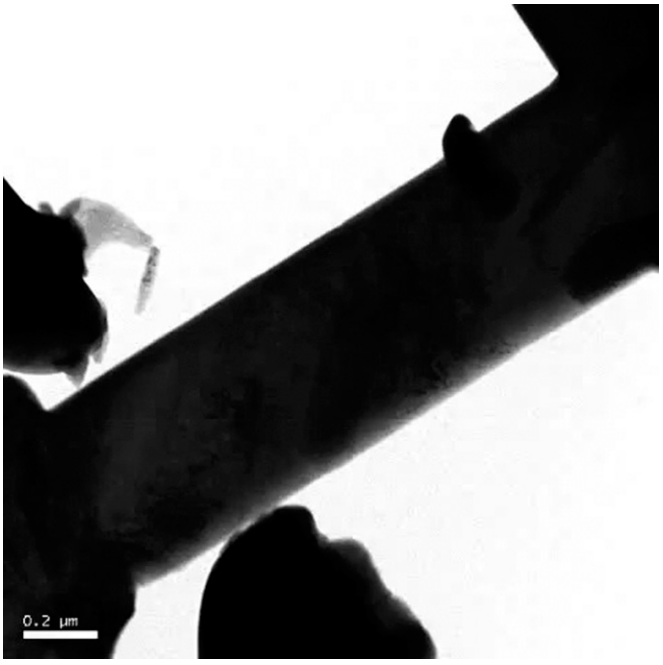

Movie S2. In situ TEM tensile test of a sample with a 600-nm gauge section.

Movie S2

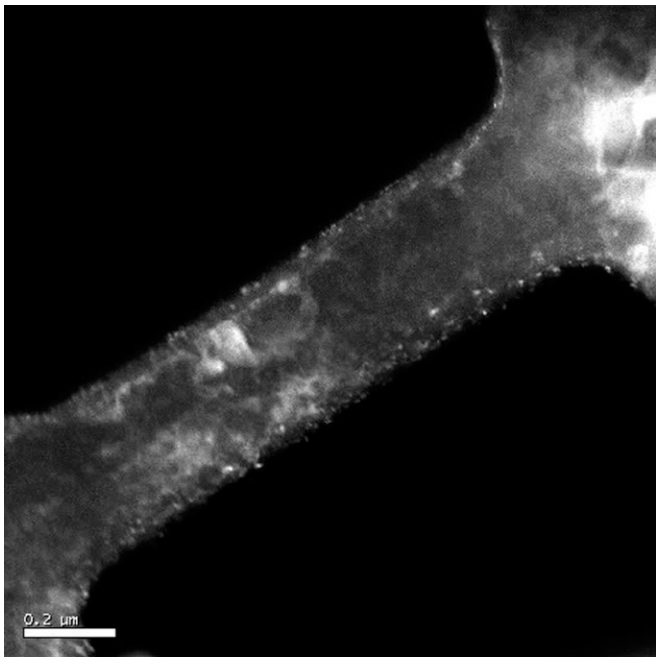

Movie S3. In situ TEM tensile test of a sample with a 280-nm gauge section.

Movie S3

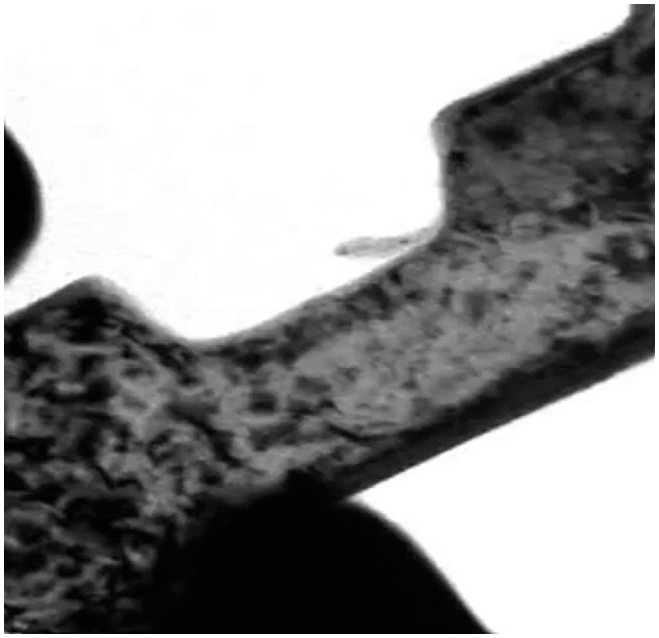

Movie S4. In situ TEM tensile test of a sample with a 100-nm gauge section.

Movie S4

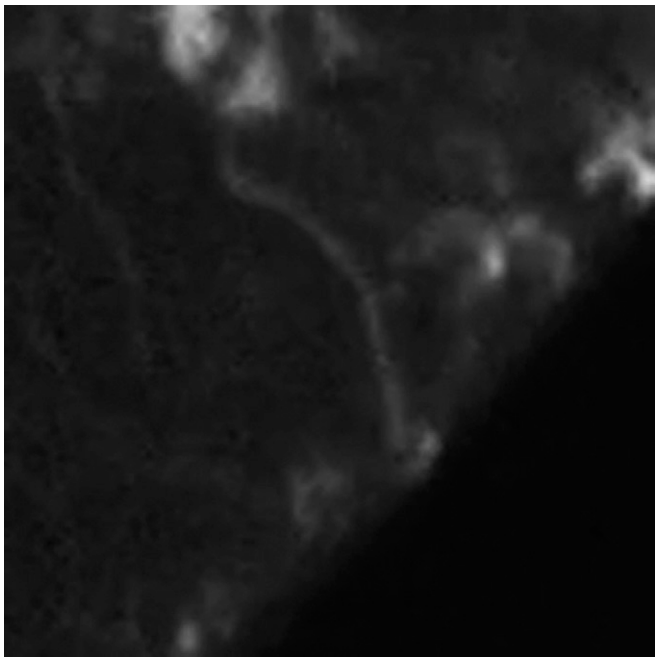

Movie S5. Portion of an in situ TEM tensile test of a sample with a 90-nm gauge section showing the pinning/depinning of a <**c** + **a**> dislocation.

Movie S5

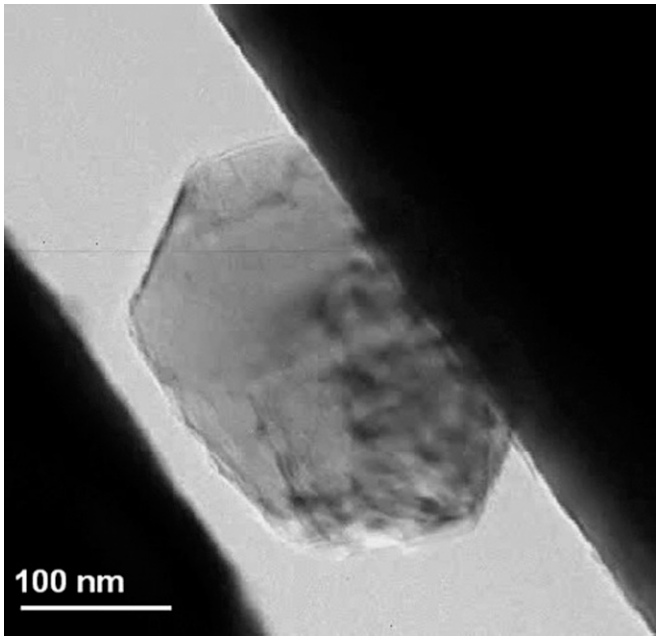

Movie S6. Large nanoparticle compression.

Movie S6

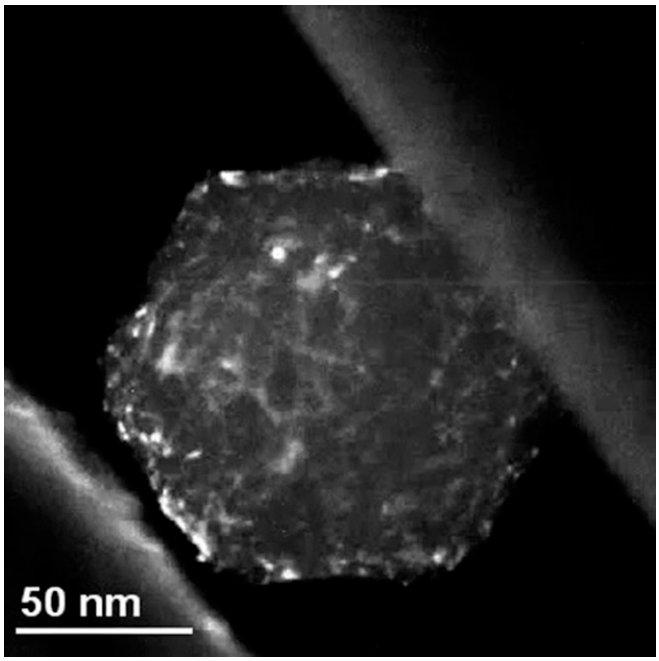

Movie S7. Small nanoparticle compression.

Movie S7

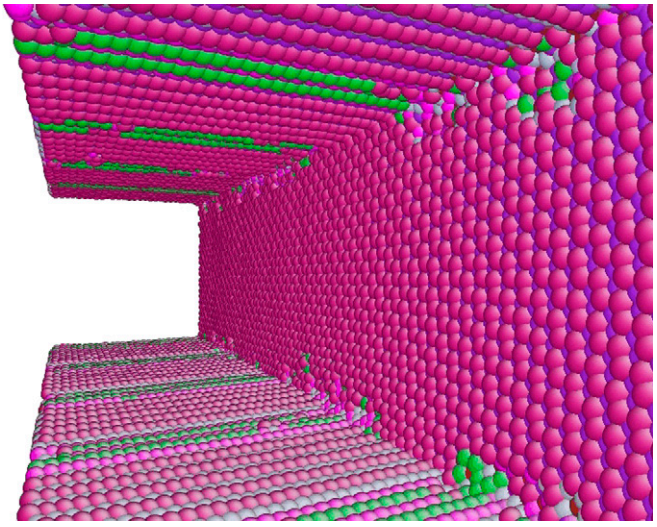

Movie S8. Dislocation activities during the tensile test in a $20 \times 20 \times 60$-nm^3 sample with type A orientation (details of lattice orientation are shown in Fig. S7). The different colors refer to different coordination numbers (CN). To illustrate clearly the dislocations inside the sample, only atoms with CN $\neq$ 12 are shown and one {01-10} surface of the sample is also removed. The applied strain increased from 0 to 0.2, with a strain rate of 2×10^7 s^{-1} so that the total deformation time was 10^{-8} s, and the atomic configuration was recorded for each 10^{-11} s. In this movie, we only show the configurations corresponding to stress drops on the stress–strain curve (Fig. 4*B*) as strain increases, because there were no dislocation activities in other configurations. Because of the recording time step (10^{-11} s), which is much larger than the MD time step (10^{-15} s), the movie does not contain all the dislocation activities during the MD simulations. Nevertheless, it still shows nucleation, propagations, and interactions of different types of dislocations. For example, Fig. 4*D* is just a snapshot of this movie at 10th second and Fig. 4*C* is the final snapshot of this movie with a different view angle.

Movie S8

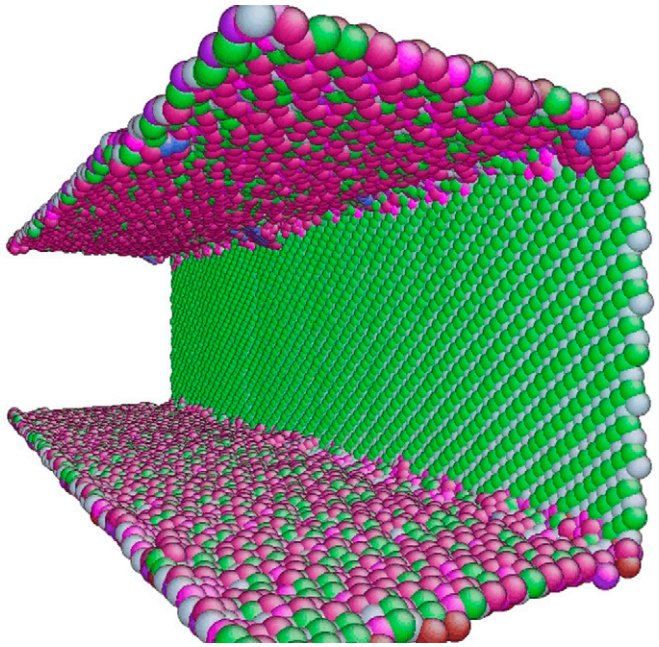

Movie S9. Dislocation nucleation at separate surface sites when stress drops at strain = 0.05 in a $10 \times 10 \times 30$-nm^3 sample with type A orientation. The setup of atom color is the same as in Movie S6. The atomic configuration was recorded for each 5.0×10^{-13} s so that every dislocation nucleation event can be shown clearly. In this movie, we can see that one pair of basal partial dislocations appears at the fifth second and another pair appears at the 22nd second at different sites.

Movie S9

BIOCHEMISTRY

Four Closure

The Ca^{2+}-binding protein calmodulin (CaM) is involved in the regulation of many membrane channels, but how it modulates permeability remains unclear. Reichow *et al.* have combined electron microscopy, structural modeling, molecular dynamics, and mutagenesis to study the interaction of the aquaporin AQP0 and CaM. Each monomer in the tetrameric AQP0 contains a water-conducting pore. Fitting crystal structures of the AQP0 tetramer and CaM into a 25 Å electron microscopic reconstruction revealed that CaM bound to the C-terminal helices of adjacent AQP0 monomers. Initially, CaM binds to one helix, and its proximity to the neighboring monomer then allows it to capture the second one. Molecular dynamics simulations suggested that, although it only links two monomers, CaM restricts the dynamics of all four monomers in the tetramer. The constriction site CSII at the cytoplasmic vestibule of the channel has been proposed to gate access. Interestingly, the AQP0 residues that were stabilized most by CaM mapped to the C-terminal helices, the base of the last transmembrane helix, and residues that form CSII. In AQP0, tetramerization is not required for water permeability; however, these results show that its quaternary structure facilitates cooperative regulation, and the regulation of other membrane channels by CaM may rely on similar mechanisms. — VV

Nat. Struct. Mol. Biol. **20,** 10.1038/nsmb.2630 (2013).

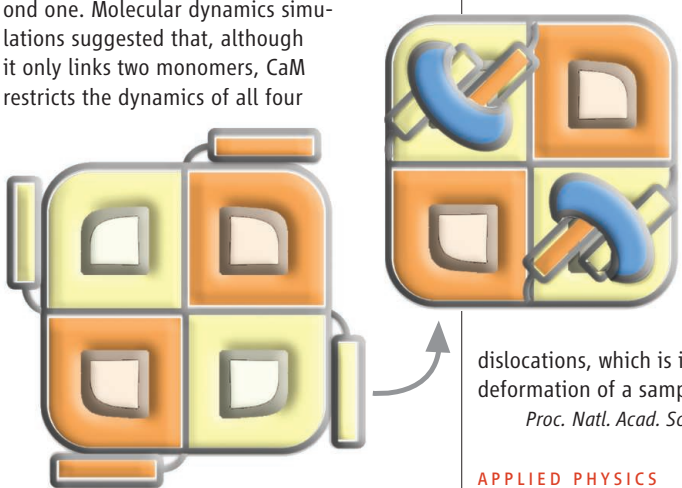

CREDIT: S. L. REICHOW *ET AL.*, *NATURE STRUCTURE & MOLECULAR BIOLOGY* **20** (28 JULY 2013) © 2013 NATURE PUBLISHING GROUP

MATERIALS SCIENCE

Making Mg Magnificent

When crystalline materials are stressed, defects in the crystal planes become mobile once a critical stress is reached. The stress required for movement of these dislocations along different slip planes can vary considerably, leading to poor ductility. Magnesium is an example of a material with an extreme anisotropy: The critical stress required for deformation along nonbasal planes is 100 times larger than along basal ones. Yu *et al.* postulated that even though materials are known to be stronger when they are smaller, there are upper bounds to this enhancement, so that the critical anisotropy should decrease. They tested single-crystal Mg samples ranging from 850 to 80 nm in size inside a quantitative electron microscope. At sizes between 200 and 400 nm, significant strengthening of the samples was seen, but the ductility remained poor. Below 100 nm, there was a shift in the deformation behavior. As the local flow stresses approached 2 GPa, there was increasing activation of the nonbasal planes, leading to a large amount of plastic deformation. These size effects could be employed to make better use of other high plastically anisotropic materials. The use of grain boundaries could allow for larger overall samples, because the boundaries will act as stress concentrators and preferred sources for the nucleation and emission of dislocations, which is important during plastic deformation of a sample. — MSL

Proc. Natl. Acad. Sci. U.S.A. **110,** 13289 (2013).

APPLIED PHYSICS

Slowly Does It

The rise and fall of pitch of a passing police siren gives a familiar example of the Doppler effect. In such a case, the speed of the moving object is appreciable compared to the speed of sound, with fast-moving objects relatively easy to detect. The situation is somewhat more difficult for slow-moving objects, where the frequency shift can be very small. Detection typically requires complex interferometry. Bortolozzo *et al.* show that a slow light medium can be used to accentuate and detect tiny frequency shifts associated with slow-moving objects. Obviating the need for complex optics, they use a balanced detection scheme where they simply split a laser beam in two and measure the intensity difference between the two beams once they pass through the slow light medium. They can detect frequency shifts down to 1 μHz and suggest that the simple setup should allow for remote sensing of slow-moving objects. — ISO

Opt. Lett. **38**, 3107 (2013).

Published by AAAS